inorganics

MDPI

Article

Near-Infrared Synaptic Responses of WSe_2 Artificial Synapse Based on Upconversion Luminescence from Lanthanide Doped Nanoparticles

Yaxian Lu, Chuanwen Chen, Qi Sun, Ni Zhang, Kun Lv, Zhiling Chen, Yuelan He, Haowen Tang and Ping Chen *

Center on Nano-Energy Research, Guangxi Key Laboratory for Relativistic Astrophysics, School of Physical Science and Technology, Guangxi University, Nanning 530004, China
* Correspondence: chenping@gxu.edu.cn

Abstract

Near-infrared (NIR) photoelectric synaptic devices show great potential in studying NIR artificial visual systems integrating excellent optical characteristics and bionic synaptic plasticity. However, NIR synapses based on transition metal dichalcogenides (TMDCs) suffer from low stability and poor environmental performance. Thus, an environmentally friendly NIR synapse was fabricated based on lanthanide-doped upconversion nanoparticles (UCNPs) and two-dimensional (2D) WSe_2 via solution spin coating technology. Biological synaptic functions were simulated successfully through 975 nm laser regulation, including paired-pulse facilitation (PPF), spike rate-dependent plasticity, and spike timing-dependent plasticity. Handwritten digital images were also recognized by an artificial neural network based on device characteristics with a high accuracy of 97.24%. In addition, human and animal identification in foggy and low-visibility surroundings was proposed by the synaptic response of the device combined with an NIR laser and visible simulation. These findings might provide promising strategies for developing a 24/7 visual response of humanoid robots.

Keywords: artificial synapse; near-infrared trigger; 2D WSe_2; upconversion

check for updates

Academic Editor: Hans Riesen

Received: 28 May 2025
Revised: 2 July 2025
Accepted: 8 July 2025
Published: 10 July 2025

Citation: Lu, Y.; Chen, C.; Sun, Q.; Zhang, N.; Lv, K.; Chen, Z.; He, Y.; Tang, H.; Chen, P. Near-Infrared Synaptic Responses of WSe_2 Artificial Synapse Based on Upconversion Luminescence from Lanthanide Doped Nanoparticles. *Inorganics* **2025**, *13*, 236. https://doi.org/10.3390/inorganics13070236

Copyright: © 2025 by the authors. Licensee MDPI, Basel, Switzerland. This article is an open access article distributed under the terms and conditions of the Creative Commons Attribution (CC BY) license (https://creativecommons.org/licenses/by/4.0/).

1. Introduction

With the development of applications in real-time pattern recognition and edge intelligence, the demand for computing efficiency is increasing rapidly. Traditional von Neumann architecture faces bottleneck problems of transmission delay and high energy consumption due to storage and computing separation [1–3]. In contrast, the human brain possesses an efficient and low-consuming superiority for integrating memory and computation with neurons and synapses to mitigate the von Neumann bottleneck [4,5]. It is worth noting that the visual system plays a leading role in external information perception. It undertakes more than 80% of the information acquisition tasks by transmitting signals from the retina to the brain via neurotransmitters [6–8]. To mimic the visual sensing function of the human brain, researchers have successfully developed photoelectric synaptic devices using various photosensitive materials such as perovskites [9], polymers [10,11], transition metal dichalcogenides (TMDCs) [12–15]. Among them, two-dimensional (2D) TMDCs attract much attention due to their perfect advantages of high carrier mobility, strong absorption of visible light, low toxicity, and high stability [16–19]. Notably, the layered structure of WSe_2 endows unique interfacial properties, demonstrating significant potential in constructing photo-responsive heterostructures. Most TMDC-based photoelectric synaptic

devices reported to date operate primarily in the visible range, as their response to the near-infrared (NIR) region is limited by the intrinsic bandgap [20–22]. Compared with visible photoelectric synapses, NIR photoelectric synapses are not limited by day and night light conditions, allowing them to work stably at night or in dark environments, which makes it possible for the collaborative application of infrared night vision systems [23]. In addition, thanks to its long-wavelength characteristics, NIR has the advantage of deeper signal penetration in haze and smoke environments. Thus, NIR photoelectric synapses can maintain stable recognition even in low-visibility environments (e.g., sandstorms or hazy weather), and have important value in key areas of autonomous driving, security monitoring, and military applications. Therefore, there is an urgent need to develop NIR photoelectric synaptic devices.

To improve the NIR response of TMDC-based photoelectric synapses, more attention has been paid to heterojunction structures, such as $CoTe_2/ZnO/WS_2$, In_2Se_3/MoS_2, and Ta_2NiSe_5/SnS_2. Ray et al. expanded the response of the TMDC synapse to 800 nm by interfacial band alignment of $CoTe_2$, ZnO, and WS_2 [24]. Hu et al. extended the NIR response to 1060 nm by constructing an In_2Se_3/MoS_2 heterostructure [25]. And Li et al. proposed a physisorption-assistant optoelectronic synapse for Ta_2NiSe_5/SnS_2 with an extended modulation at 1310 nm [26]. Yet, the complex preparation process and sensitivity of light and water make it difficult to control interface defects and environmental sensitivity. Another method was explored with lanthanide-doped upconversion nanoparticles (UCNPs) and 2D TMDC nanosheets. UCNPs convert low-energy NIR photons into high-energy visible or ultraviolet light by an upconversion process, which could be absorbed by TMDCs. Thus, the light response range of TMDCs was expanded to NIR. Han et al. proposed a NIR neuromorphic computing based on UCNP-sensitized MoS_2 nanocomposites floating gate dielectric with pentacene as the semiconductor channel [27]. Long-term potentiation and depression (LTP/D) were achieved for the first time with an accuracy of 70% in handwritten character recognition tasks. However, the MoS_2 nanosheets reduced the transport performance and the sensitivity of pentacene to light and air, also confining the practical applications. Thus, it is urgent to improve the NIR response of TMDC-based photoelectric synapses with a simple process and good stability.

In this work, we constructed a novel UCNPs-WSe_2 optoelectronic synapse device based on upconversion luminescence (UCL) from lanthanide-doped nanoparticles with spin-coating UCNPs on the surface of WSe_2, which extends the photoresponse to 975 nm. Direct spin-coating of UCNPs onto large-area WSe_2 ensures continuous WSe_2 channels to avoid discontinuous electrical transportation. Meanwhile, direct contact between WSe_2 and UCNPs reduces the sensitivity of organic linkers. The prepared synaptic device successfully simulated core biological synaptic functions, including paired-pulse facilitation (PPF), spike rate-dependent plasticity, and spike timing-dependent plasticity. Then, the handwritten digit recognition was achieved with 97.24% accuracy on the basis of two types of LTP in UCNPs-WSe_2 optoelectronic synapse. Moreover, a dual-mode scheme was proposed to identify the target in foggy environments. These findings provide an innovative solution for autonomous driving, industrial inspection, and disaster relief.

The prepared synaptic device successfully simulated core biological synaptic functions, including paired-pulse facilitation (PPF), spike rate-dependent plasticity, and spike timing-dependent plasticity. Then, the handwritten digit recognition was achieved on the basis of two types of LTP in UCNPs-WSe_2 optoelectronic synapse. Moreover, a dual-mode scheme was proposed to identify the target in foggy environments. These findings provide an innovative solution for autonomous driving, industrial inspection, and disaster relief.

2. Results and Discussion

2.1. NIR-Responsive Artificial Synapse

In biological neural networks, synapses, as the functional basis unit, can enhance synaptic connections by conducting neurotransmitters released by presynaptic neurons and generate excitatory postsynaptic current (EPSC). Taking the human retina as an example, this biological structure can transmit external light signals to the brain through neurotransmitters to store and process (Figure 1a(i)) [28]. However, the biological retina cannot directly perceive NIR stimulation due to the light response range of opsin. To enhance NIR response, an artificial UCNPs-WSe_2 optoelectronic synaptic device (Figure 1b) was constructed. Those NIR responsive synapses will help to recognize the kitten silhouettes if a robot is equipped with this device (Figure 1a(ii)). Under the condition of light response characteristics of the NIR band regulated by UCNPs and the visible region responded to by WSe_2, the simulated robot system can adapt to the all-weather environment of super bionic vision.

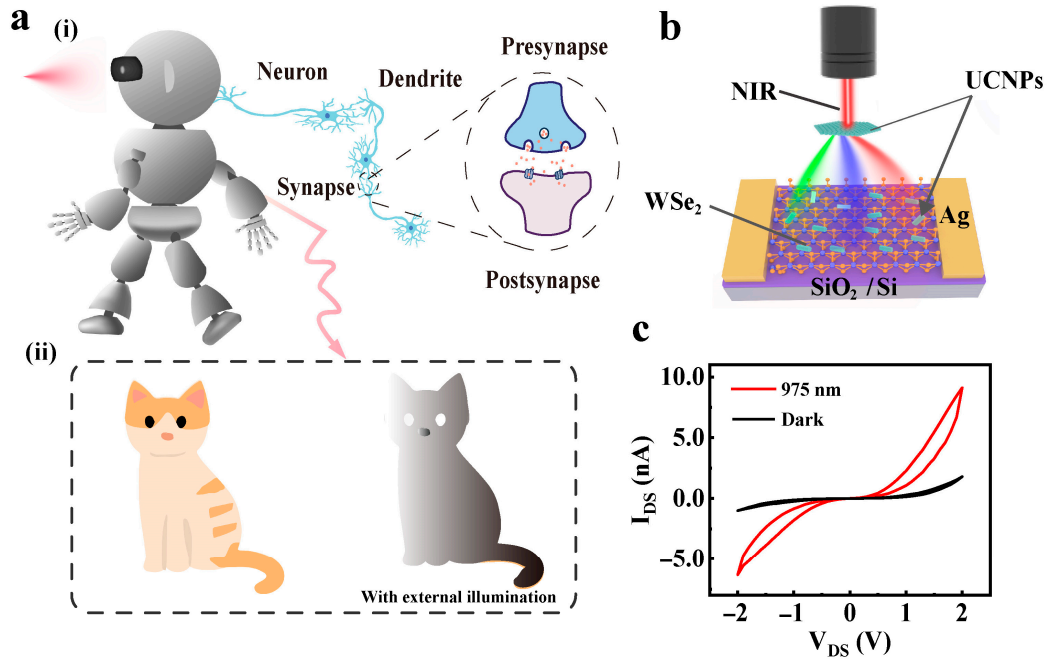


Figure 1. Upconversion-mediated NIR photoelectric synaptic device for super-bionic vision with all-weather adaptability. (**a**) Schematic of the bionic robot's visual recognition system, (**i**) Neuronal and synaptic structure during target recognition, (**ii**) Simulation of continuous kitten silhouette recognition under visible and NIR illumination. (**b**) Schematic structure of the UCNPs-WSe_2 optoelectronic device. (**c**) Current–Voltage (I-V) characteristics measured in the dark and under 975 nm illumination.

Figure 1b shows a schematic diagram of the UCNPs-WSe_2 photoelectric synaptic device. When the device is irradiated with NIR, the visible light emitted from UCNPs excited by 975 nm is reabsorbed by WSe_2 to achieve precise modulation of NIR synaptic performance. By characterizing the WSe_2 material prepared by physical vapor deposition (PVD), it can be seen that the synthetic WSe_2 is a homogeneous and high-quality crystalline material with a bilayer structure, as shown in Figure S1. To study the synaptic characteristics of the device, we first conducted an output performance test. Figure 1c shows the output hysteresis curve of the UCNPs-WSe_2 device under the dark and 975 nm states, which indicates the synaptic potential. Compared with dark conditions, the 975 nm irradiation hysteresis window was significantly larger. This improved performance originated from the UCL effect of UCNPs, which activates WSe_2 photoresponse characteristics. Higher carrier concentrations enhanced the probability of capturing electrons, leading to longer electron

release during backward scanning and a larger hysteresis window. And the defect-state in WSe_2 enhanced the carrier capture/release effect. This phenomenon suggests that devices play a greater role in regulating synaptic plasticity under NIR irradiation.

2.2. Mechanism Analysis of UCNPs-WSe_2 Synaptic Device

To gain an in-depth understanding of the working mechanism of UCNPs-WSe_2 synaptic devices, we considered the schematic diagram of the energy levels (Figure 2). Figure 2a shows the energy band diagram of Ag and WSe_2. Before contacting (Figure 2a), the work function (W_m) of Ag is 4.2 eV, and the electron affinity (χ_s) of WSe_2 is 4.0 eV [29–31]. The bandgap (E_g) of WSe_2 is 1.59 eV [32]. Because of the p-type semiconductor characteristics of WSe_2, according to the transfer characteristic curve in Figure S2, the Fermi level is located near the valence band. When Ag is in contact with WSe_2, electrons from Ag are injected into WSe_2, resulting in bending of the WSe_2 surface energy band, as shown in Figure 2b. When a forward bias is applied, the potential gradient between the source (left) and the drain (right) causes the semiconductor energy band to gradually tilt downward from the source to the drain [33–35]. Under this bias voltage, the holes in the valence band and electrons in the conduction band migrate to the source and drain electrodes along the inclined energy band, respectively. For deep energy-level traps formed by Se vacancy defects in WSe_2, lots of electrons are captured. And the captured electrons will be rereleased when thermal excitation or an electric field drives them. The difference in relaxation times during the capture–release process results in a hysteresis of current response [12], consistent with the test results in the dark conditions of Figure 1c. As shown in Figure 2c, under light conditions, photons will generate electron–hole pairs, leading to a higher current. Meanwhile, part of the photons generated electrons in the conduction band are captured by the Se vacancy defects, and their dynamic capture–release process results in the redistribution of the interface carriers, ultimately causing the device to present a larger hysteresis window (red curve in Figure 1c).

To explain the energy transfer mechanism between WSe_2, UCNPs-WSe_2 and UCNP absorption and photoluminescence (PL) spectra of WSe_2, UCNPs, and UCNPs-WSe_2 composites were characterized. Two absorption peaks at 595 nm and 762 nm were detected, corresponding to A and B exciton resonance characteristics (Figure 2d) [36,37], and indicating the strong absorption capacity of the material in the visible light region. An absorbed band around 980 nm was presented from $NaYF_4$: 20%Yb, 0.5%Tm UCNPs, originating from the $^2F_{7/2} \rightarrow {}^2F_{5/2}$ transition of Yb^{3+}, and a weak absorption peak at 980 nm was observed in UCNPs-WSe_2 composites, suggesting the potential of an NIR response of the UCNPs-WSe_2 device. Further, PL spectra were conducted to reveal the effects of UCNPs on 2D WSe_2 (Figure S3), showing no significant effect of UCNPs on the luminescent properties of WSe_2. Notably, UCNPs exhibit emission peaks of Tm^{3+} at 452 nm, 476 nm, 648 nm, 695 nm, and 792 nm, upon excitation by 980 nm, corresponding to the transitions of $^1D_2 \rightarrow {}^3F_4$, $^1G_4 \rightarrow {}^3H_6$, $^1G_4 \rightarrow {}^3F_4$, $^3F_3 \rightarrow {}^3H_6$, and $^3H_4 \rightarrow {}^3H_6$, respectively (Figure 2e) [38]. Notably, the luminescence intensity of these emission peaks was significantly reduced or even completely quenched when UCNPs were composited with 2D WSe_2, indicating an efficient energy transfer from UCL of UCNPs to WSe_2 [39]. Figure 2f shows the schematic diagram of UCL from Yb^{3+} to Tm^{3+} and energy transfer to WSe_2. When 975 nm NIR is applied, Yb^{3+} ions effectively absorb 975 nm photons from the ground state $^2F_{7/2}$ to the excited state $^2F_{5/2}$, then transfer energy to the excited state $^3H_5$ of Tm^{3+}, followed by relaxation to $^3F_4$ state by non-radiative relaxation. And the $^3F_4$ state of Tm^{3+} will be pumped to the $^3F_{2,3}$ excited states after transferring the second photon energy from Yb^{3+}. Thereby, $^1G_4$ and $^1D_2$ states will be generated after absorbing the third and fourth photon energy from Yb^{3+}. And radiative transitions from the $^1G_4$ and $^1D_2$ states provided visible luminescence around

452 nm, 476 nm, 648 nm with $^1D_2 \rightarrow {}^3F_4$, $^1G_4 \rightarrow {}^3H_6$, $^1G_4 \rightarrow {}^3F_4$ transitions, respectively. Meanwhile, the visible luminescence was reabsorbed by WSe_2 by radiative reabsorption, enabling the NIR response of WSe_2. This multi-level energy regulation lays the physical foundation for the bionic modulation function of photo-controlled synaptic devices.

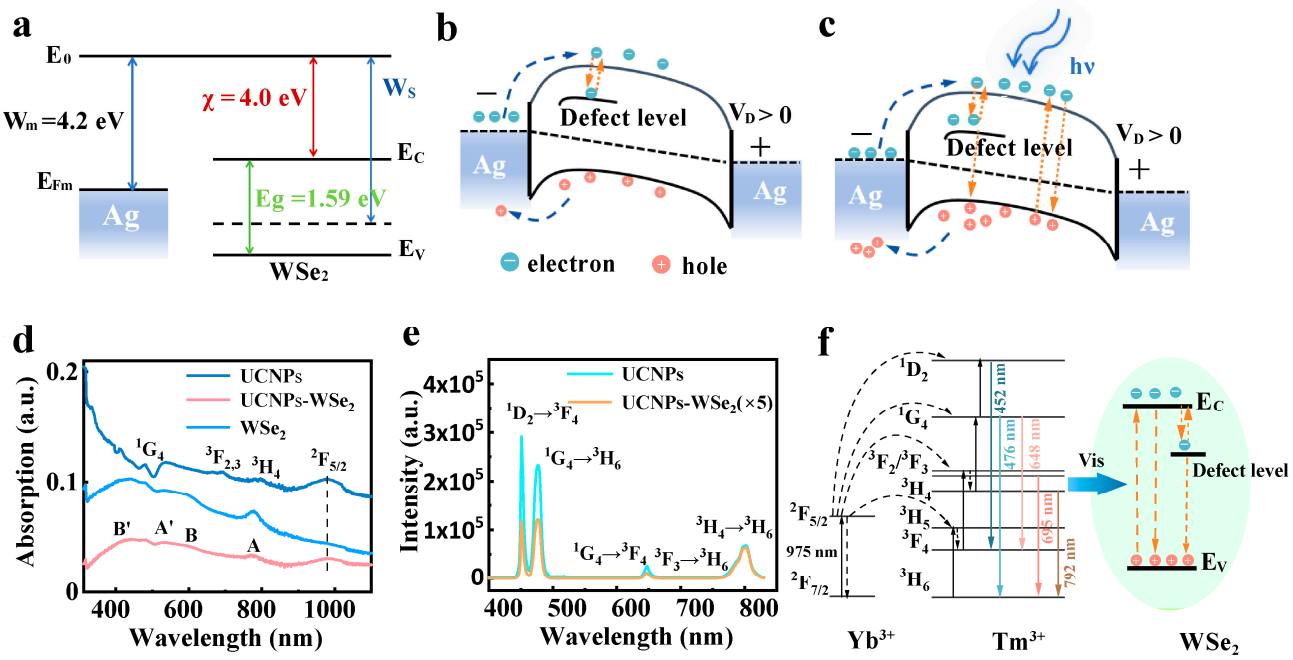


Figure 2. Working mechanism and optical properties of the UCNPs-WSe_2 synaptic device. (**a**) Schematic diagram of the energy level before contact between WSe_2 and Ag. The blue line shows the work function, the red line shows the electron affinity and the green line shows bandgap. (**b**) Energy band structure of WSe_2 and Ag under dark conditions and (**c**) under visible illumination. (**d**) Absorption spectra of WSe_2, UCNPs-WSe_2 and UCNPs. The dashed line shows that the same absorption of UCNPs and UCNPs-WSe_2. (**e**) PL spectra of UCNPs and UCNPs-WSe_2 (×5) under 980 nm laser excitation. (**f**) Schematic diagram of UCL from Yb^{3+} to Tm^{3+} and energy transfer to WSe_2.

2.3. Properties of UCNPs-WSe_2 Synaptic Device

Based on the fact that WSe_2 can effectively absorb the visible light emitted by UCNPs, the synaptic function of the UCNPs-WSe_2 device was simulated with the excitation at 975 nm. The detailed mechanism of optical energy transfer to synaptic electroplasticity is shown in Figure S4. When the NIR pulse was applied, the device produced a typical EPSC response. Single-pulse-triggered EPSC under different power and pulse width conditions was increased significantly with higher optical power density and longer pulse width (Figures 3a,b and S5a,b). In addition, compared with the WSe_2 device without spin-coating, the photoresponse was significantly enhanced after spin-coating UCNPs (Figure S6), which demonstrated that the bandgap mismatch between WSe_2 and NIR was effectively overcome.

PPF is another typical short-term potentiation (STP) behavior that is conducive to the signal transmission efficiency between neurons. When two consecutive pulses were applied, the second pulse caused a greater change in synaptic weight than the first one. This was attributed to the increased synaptic weight due to the failed recovery of carriers to their initial states within the time interval. Here, PPF behavior was demonstrated successfully

under two 975 nm pulses with a width of 3 s and an interval of 1 s. The PPF index was defined and calculated by the following formula [40–43]:

$$\text{PPF index} = \frac{A_2}{A_1} \times 100\% \quad (1)$$

where A_1 and A_2 represent the ΔEPSC amplitudes triggered by the first and second pulses, respectively. PPF reached a maximum of 160.15% with a time of 23 s. The correlation between the PPF index and time interval can be fitted using the bi-exponential equation (Figure 3c) [40]:

$$\text{PPF index} = 1 + B_1 \times \exp\left(-\frac{\Delta t}{\tau_1}\right) + B_2 \times \exp\left(-\frac{\Delta t}{\tau_2}\right) \quad (2)$$

where B_1 and B_2 are the initial excitation amplitudes, τ_1 and τ_2 are the fast and slow characteristic relaxation times during decay, respectively. The calculated τ_1 and τ_2 values are 4.38 s and 84.24 s, respectively, which are consistent with the characteristics of biological synapses [44].

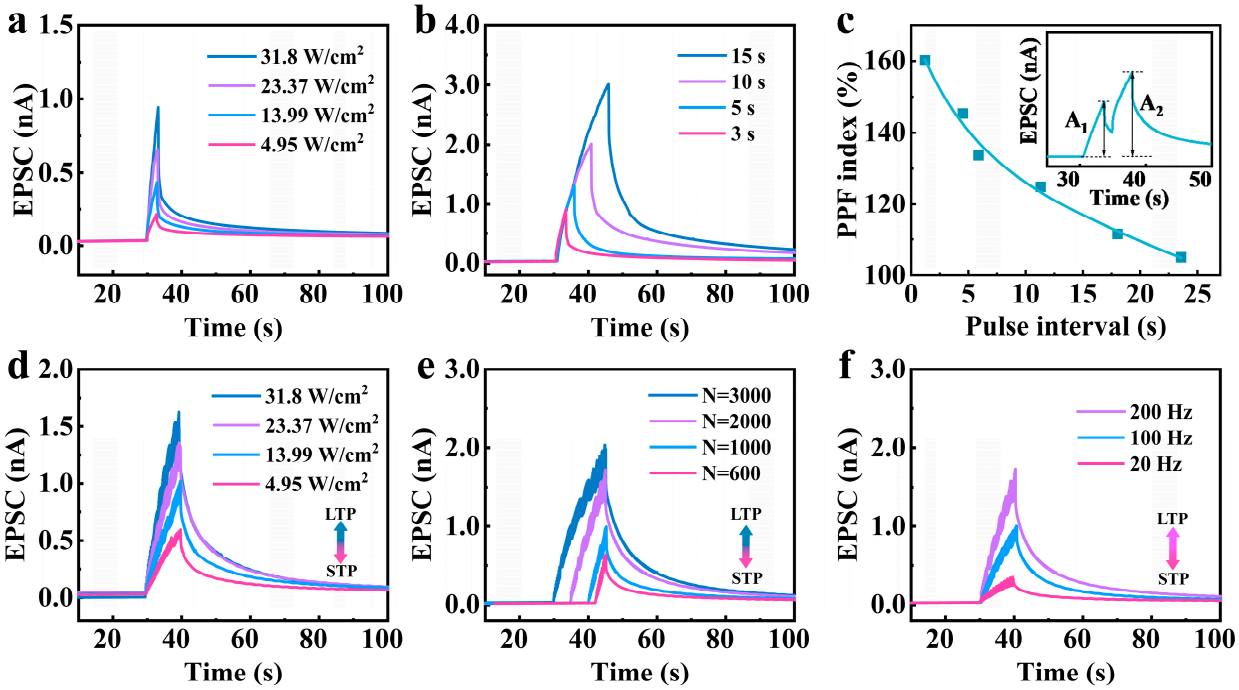


Figure 3. NIR synaptic plasticity of the UCNPs-WSe_2 device. (**a**) EPSC triggered by a single 975 nm pulse (width 3 s) at varying power densities. (**b**) EPSC modulated by a single 975 nm pulse with different widths under the condition of power density 31.8 W/cm^2. (**c**) PPF index as a function of pulse interval. Inset: EPSC response to paired pulses (31.8 W/cm^2, width 3 s, interval 1 s). (**d**) LTP was induced by 2000 consecutive optical pulses at different power densities (width 2.5 ms, interval 2.5 ms). (**e**) EPSC triggered by 600, 1000, 2000, and 3000 light pulses (31.8 W/cm^2, width 2.5 ms, interval 2.5 ms). (**f**) Frequency-dependent EPSC with 2000 light pulses (31.8 W/cm^2). All measurements were performed under a 100 mV voltage.

The transformation from STP to LTP is of great significance to the development of neuromorphic computing systems with adaptive learning capabilities. This is because STP mainly implements dynamic signal coding and temporary information cache, while LTP is a persistent change, providing the basis for long-term memory storage and neural network function reshaping. Therefore, synaptic plasticity was investigated with different power densities, numbers, and frequencies of light pulses (Figures 3d–f and S7). The transition of

EPSC amplitude from STP to LTP was realized by increasing incoming light intensity from 4.95 to 31.8 W/cm^2, the number of pulses from 600 to 3000, and pulse frequency from 20 to 200 Hz. The fundamental reason for this is that larger light intensity/pulse numbers/pulse frequency induces a larger concentration of carriers in 2D WSe_2, resulting in capturing more electrons in defective states and a longer recovery [12,45,46].

2.4. Learning Experience Behavior and Handwritten Digital Image Recognition

A UCNPs-WSe_2 synapse can simulate learners' characteristics triggered by 975 nm pulses (Figure 4a), where the learning–forget–release process can be achieved. After applying 4000 pulses, ΔEPSC increased from 0 to 2.23 nA, corresponding to the first learning process (i). When the pulses were removed, ΔEPSC was attenuated to 0.75 nA within 7 s, representing the forgetting process (ii). In the re-learning phase (iii), only 1600 pulses were required to achieve the same ΔEPSC triggered by the 4000 pulses in the first learning phase.

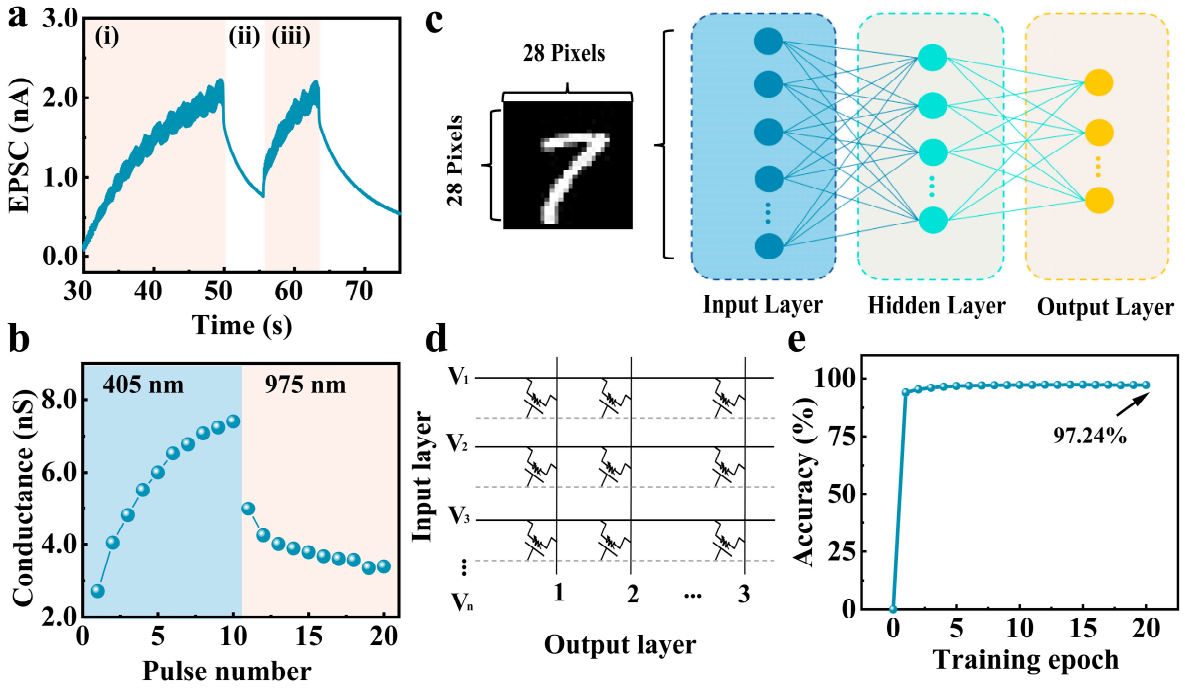


Figure 4. Human learning behavior and handwritten digit recognition by ANN-based behavior UCNPs-WSe_2 synaptic weights. (**a**) Learning behavior triggered by 975 nm light pulses (31.8 W/cm^2, width 2.5 ms, interval 2.5 ms). (i)–(iii) shows the EPSC under (i) 4000 pulses (ii) dark environment (iii) 1600 pulses, respectively. (**b**) Conductance changes modulated by 405 nm and 975 nm. (**c**) Schematic of the three-layer ANN used to recognize MNIST images. (**d**) Cross-switch array structure. (**e**) Dependence of recognition accuracy on training rounds.

An artificial neural network (ANN) for handwritten digit recognition was constructed based on the synaptic plasticity of the device in the Vis-NIR range. According to the strong absorption characteristics of WSe_2 in the visible range [47], the synaptic performance of the UCNPs-WSe_2 device was modulated by 405 nm visible light (Figures S8 and S9). The synaptic weights were regulated by timing-controlled 405 nm and 975 nm NIR pulses. First, 10 pulses at 405 nm (26.68 mW/cm^2, width 0.5 s) were applied, followed by 10 975 nm pulses (27.84 W/cm^2, width 1 s). Conductance values were extracted by simulating the continuous variation of LTP with the timing of the two wavelength pulses (Figure S10). The successful simulation of two types of LTP by optical pulses highlights its unique advantages in the field of photo-controlled synaptic bionics. Then, a three-layer ANN was constructed containing 784 input neurons, 300 hidden neurons, and 10 output

neurons, as shown in Figure 4c. Training and recognition of 28 × 28 pixel handwritten digits from the Modified National Institute of Standards and Technology (MNIST) database were performed using the CrossSim simulator. During the training process, 784 input neurons corresponded to a handwritten digital image, while 10 output neurons matched 10 numbers (0–9). The single-layer structure of the network performs vector matrix multiplication and sum operations by mapping the cross-switch array hardware (Figure 4d) to achieve efficient computing, thereby enabling large-scale parallel signal processing. As shown in Figure 4e, the recognition accuracy corresponding to the regulated synaptic weights in Figure 4b increases gradually with the increase in training rounds. The accuracy rate finally reached 97.24% after 20 training rounds, giving great potential in the field of neuromorphic vision.

2.5. Possible Application Directions of UCNPs-WSe_2 Device

Inspired by the sensing and information processing mechanism of the viper's vision system, the identification of birds in a day–night environment was proposed according to visible and NIR response characteristics of the UCNPs-WSe_2 photoelectric synaptic device by setting the recognition EPSC threshold. In viper's vision system, NIR and visible signals are integrated through neural integration to generate dynamic thermal imaging maps, allowing them to achieve millimeter-level spatial positioning in day–night environments, which is particularly prominent when tracking mobile targets [48–50]. The threshold for "recognized" and "unrecognized" was set based on test results. For the identification of birds in daytime mode, when 405 nm pulsed light (26.68 mW/cm^2, width 3 s) was applied, the EPSC of UCNPs-WSe_2 synapse exceeded the preset threshold, indicating that the capability of identifying the bird (Figure 5a(i),b). When the environment switches to night mode, the system automatically enables the NIR sensing mechanism. The induced EPSC of UCNPs-WSe_2 synapse also reached the recognition threshold triggered by NIR 975 nm laser (31.8 W/cm^2, width: 3 s), which shows no response to a 36 °C living body.

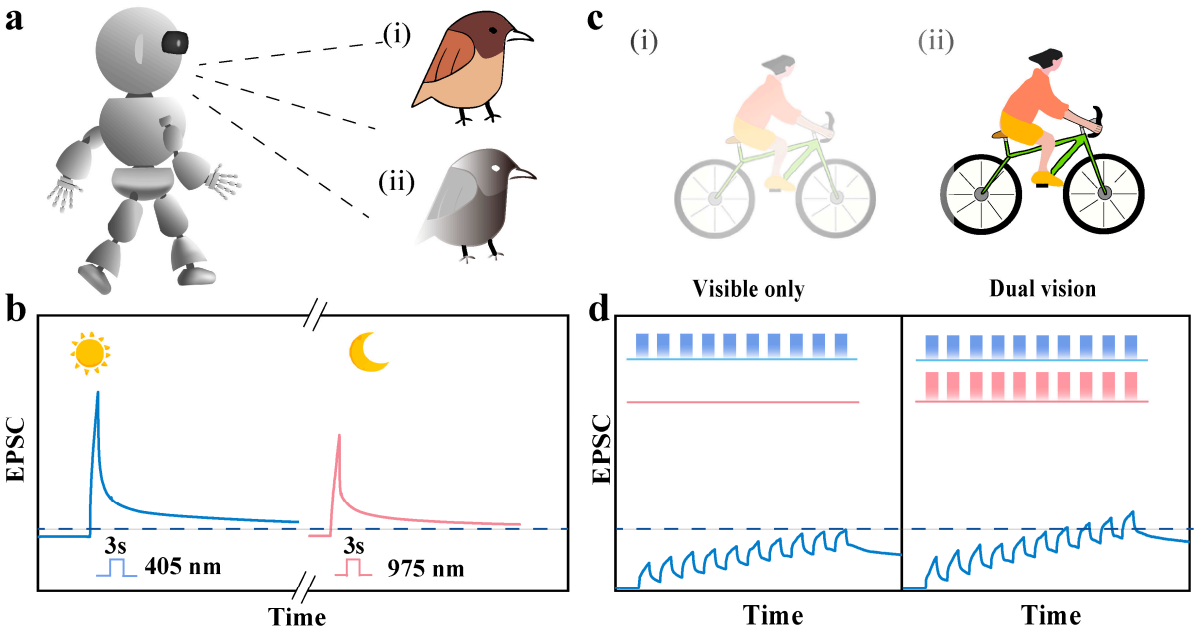


Figure 5. A proposed simulation of a bionic robot with all-weather recognition. (**a**) Identification of bird recognition by the bionic robot during (**i**) day and (**ii**) night with preset thresholds. (**b**) 405 nm (**left**) and 975 nm laser (**right**) single pulse triggered EPSC. (**c**) Identification of a biker recognition in a foggy environment with (**i**) a visible single-mode and (**ii**) a visible and NIR dual-mode. (**d**) EPSC of UCNPs-WSe_2 synapse triggered by 405 nm (**left**), 405 nm and 975 nm laser (**right**). Blue (405 nm) and red (975 nm) curves correspond to pulsed lights of different wavelengths, and the dashed line represents the preset threshold.

Then, the robot's recognition of riders on a foggy day was proposed, triggered by visible and NIR pulses. The threshold for "recognized" and "unrecognized" was set based on test results. The EPSC intensity in visible mode is lower than the preset recognition threshold, causing failure to identify the rider, as shown in Figure 5c(i),d(left). By combining NIR excitation, the EPSC intensity exceeded the threshold, enabling clear contour recognition of the rider (Figure 5c(ii),d(right)). This dual-mode optical fusion strategy allows robot vision systems to maintain robust recognition capabilities under harsh conditions.

3. Materials and Methods

3.1. WSe_2 Synthesis

The 2D WSe_2 was grown by PVD [51]. High-purity WSe_2 powder (99.9%, Alfa Aesar, Shanghai, China) was placed in a quartz boat as raw material and placed in the center of a 1-inch quartz tube. The 285 nm SiO_2/Si substrate (Lijing Electronics Co., Ltd., Shenzhen, China) was placed 20 cm downstream from the raw material. At a continuous rate of 20 sccm Ar (99.999%, Wangzhou Gas Co., Ltd, Nanning, China), the tube furnace was heated to 1185 °C for 5 min. Then, the furnace temperature was naturally cooled to room temperature.

3.2. Preparation of UCNPs ($NaYF_4$: 20%Yb^{3+}, 0.5%Tm^{3+})

UCNPs were synthesized by the hydrothermal method [52]. For this, 0.3 g sodium hydroxide (99.99%, Sigma-Aldrich, St. Louis, MO, USA) was first weighed and dissolved in 1.5 mL of deionized water. Subsequently, 5 mL of oleic acid (90%, Sigma-Aldrich, St. Louis, MO, USA) and anhydrous ethanol were added as additives, and the mixture was thoroughly mixed using a magnetic stirrer. Then, 2 mmol of ammonium fluoride solution (99.99%, Sigma-Aldrich, St. Louis, MO, USA) was added to the mixture and stirred to form a turbid suspension. Note: Ammonium fluoride had been weighed in advance and dissolved in 1 mL of deionized water for later use. Next, 0.4 mmol, 2 mL of rare earth nitrate solutions including $Y(NO_3)_3$ $6H_2O$, $Yb(NO_3)_3$ $6H_2O$, and $Tm(NO_3)_3$ $6H_2O$ (99.999%, Sigma-Aldrich, St. Louis, MO, USA), respectively, were added to the mixed solution, and the mixture was stirred for 20 min. Finally, the mixed solution was transferred into a 50 mL polytetrafluoroethylene-lined bottle, placed in a stainless steel reactor, and maintained in a constant-temperature drying oven (DHG-9076A, Shanghai Jinghong Experimental Equipment Co., Ltd, Shanghai, China) at 220 °C for 12 h. The synthesized rare earth ion-doped nanocrystals were washed three times with alcohol and cyclohexane, centrifuged (TG16-WS, Changsha Xiangrui Centrifuge Co., Ltd., Changsha, China), and dried in a constant-temperature oven at 60 °C for 6 h.

3.3. UCNPs-WSe_2 Composite Material

The prepared UCNPs were placed in a beaker, and ultra-pure water was added. The mixture was then subjected to ultrasonic treatment for 5 min to uniformly disperse the nanocrystals. Subsequently, the UCNP dispersion was spin-coated onto the 2D WSe_2 surface.

3.4. Fabrication of Transistor

The device was fabricated by applying silver paste on both sides of the material by a probe, followed by high-temperature curing to form electrodes.

3.5. Characterization

The morphology of the synthesized 2D WSe_2 was characterized using field-emission scanning electron microscopy (FE-SEM, Zeiss, Sigma500, Oberkochen, Germany), optical microscopy (OM, Olympus, BX43F, Tokyo, Japan), and atomic force microscopy (AFM,

Bruker Dimension Icon, Shah Alam, Malaysia). Raman spectra were collected with a confocal Raman spectrometer (Horiba, iHR550, Loos, France) equipped with a 532 nm laser excitation source. Photoluminescence spectra were recorded using a steady-state/transient fluorescence spectrometer (FLS-1000, Edinburgh Instruments, Livingston, UK). Absorption spectra were measured by a fluorescence spectrophotometer (Agilent, Cary Eclipse, Santa Clara, CA, USA). A 975 nm laser source (LE-LS-975-5000TFCA, Shenzhen, China) was employed for optical excitation. Device performance tests were conducted on a probe station (Lake Shore TTPX, Westerville, OH, USA) integrated with a semiconductor parameter analyzer (Keithley, 4200A-SCS, Solon, OH, USA). All characterizations were performed at room temperature.

4. Conclusions

This paper achieved a NIR responsive synapse made of 2D WSe_2 and $NaYF_4$: 20%Yb, 0.5%Tm nanocomposites. The NIR response of the synaptic device originated from the radiation reabsorption from UCL of $NaYF_4$: 20%Yb, 0.5%Tm nanoparticles to 2D WSe_2, which was confirmed by absorption and luminescence spectra. The synaptic plasticity was regulated by power density, pulse width, and pulse frequency of NIR and visible bands. Handwritten digit image recognition was realized in artificial neural networks with an accuracy rate of 97.24% based on two types of LTP synapses by constructing a coordinated regulation strategy of 405 nm and 975 nm NIR. In addition, robotic visual perception in day–night and foggy environments was proposed according to the strong absorption in the visible region and the penetration ability of NIR. This work might provide an innovative technological path for the development of all-weather intelligent sensing systems with environmental adaptability.

Supplementary Materials: The following supporting information can be downloaded at: https://www.mdpi.com/article/10.3390/inorganics13070236/s1, Figure S1: Characterization of 2D WSe_2 Materials. Figure S2: Transfer characteristic curve of WSe_2. Figure S3: Characterisation of PL spectra. (a) WSe_2. (b) UCNPs-WSe_2. (c) UCNPs. Excited by 532 nm. Figure S4: Working mechanism of UCNPs-WSe_2 device. Se vacancys capture electron situation under (a) initial state (b) single pulse (c) double pulse (d) multiple pulse irradiation. Figure S5: Extraction results of EPSC peaks of UCNPs-WSe_2 synaptic device under 975 nm excitation with (a) different power densities and (b) pulse widths. Figure S6: EPSC generated by WSe_2 synaptic device with (a) Without spin-coated UCNPs. (b) Spin-coated UCNPs on quartz. (c) Spin-coated UCNPs. Figure S7: Extracted EPSC of UCNPs-WSe_2 synaptic device under 975 nm illumination with (a) different power densities, (b) pulse widths and (c) pulse frequencies. Figure S8: Synaptic response of UCNPs-WSe_2 synaptic device under 405 nm excitation. (a) I-V curves under darkness and 405 nm illumination with different power densities. (b) EPSC triggered by a 405 nm pulse with 1 s width at different powers. (c) EPSC triggered by 405 nm pulse of different pulse durations. (d) PPF caused by a pair of 405 nm light pulses with 1 s width and 0.5 s pulse intervals. (e) The dependence of PPF index on pulse intervals. (f) EPSC induced by 10 pulses at different power densities. All measurements are performed at 100 mV voltage. Figure S9. Synaptic response of UCNPs-WSe_2 synaptic device under 405 nm excitation. (a) EPSC triggered by 405 nm with various numbers of pulses. (b) EPSC triggered by different pulse widths with time intervals of 0.5 s. (c) EPSC with frequency from 0.1 Hz to 0.25 Hz. (d) The human body's learning–forgetting–relearning behavior under 405 nm pulses. Figure S10: Two types of LTP inputs were modulated by 405 nm and 975 nm pulses under a reading voltage of 100 mV.

Author Contributions: Conceptualization, Y.L. and P.C.; data collection, Y.L., C.C., N.Z., K.L., H.T. and Y.H.; data interpretation, Y.L., P.C., Q.S. and Z.C.; writing—original draft preparation, Y.L.; writing—review and editing, Y.L. and P.C. All authors have read and agreed to the published version of the manuscript.

Funding: This study was financially supported by the Guangxi Natural Science Foundation (No. 2025GXNSFAA069357), National Natural Science Foundation of China (No. 52472153), the special fund for "Guangxi Bagui Scholars," National Science and Technology Innovation Talent Cultivation Program (No. 2023BZRC016).

Institutional Review Board Statement: Not applicable.

Informed Consent Statement: Not applicable.

Data Availability Statement: The original contributions presented in this study are included in the article and Supplementary Materials. Further inquiries can be directed to the corresponding author.

Conflicts of Interest: The authors declare no conflicts of interest.

References

1. Merolla, P.A.; Arthur, J.V.; Alvarez Icaza, R.; Cassidy, A.S.; Sawada, J.; Akopyan, F.; Jackson, B.L.; Imam, N.; Guo, C.; Nakamura, Y.; et al. A Million Spiking-Neuron Integrated Circuit with a Scalable Communication Network and Interface. *Science* **2014**, *345*, 668–673. [CrossRef]
2. Muir, D.R.; Sheik, S. The Road to Commercial Success for Neuromorphic Technologies. *Nat. Commun.* **2025**, *16*, 3586. [CrossRef]
3. Wu, W.Q.; Wang, C.F.; Han, S.T.; Pan, C.F. Recent Advances in Imaging Devices: Image Sensors and Neuromorphic Vision Sensors. *Rare Met.* **2024**, *43*, 5487–5515. [CrossRef]
4. Liang, Y.; Li, H.; Tang, H.; Zhang, C.; Men, D.; Mayer, D. Bioinspired Electrolyte-Gated Organic Synaptic Transistors: From Fundamental Requirements to Applications. *Nano-Micro Lett.* **2025**, *17*, 198. [CrossRef] [PubMed]
5. Kudithipudi, D.; Schuman, C.; Vineyard, C.M.; Pandit, T.; Merkel, C.; Kubendran, R.; Aimone, J.B.; Orchard, G.; Mayr, C.; Benosman, R.; et al. Neuromorphic Computing at Scale. *Nature* **2025**, *637*, 801–812. [CrossRef] [PubMed]
6. Lian, H.; Wang, S.; Qin, Z.; Dou, Z.; Cheng, X.; Lan, G.; Li, X.; Liu, A.; Dong, Q. Transparent and Flexible Organic Bulk Heterojunction Photonic Synapse for Neuromorphic Computing and Reflex Arc Behavior. *Device* **2025**, 100749. [CrossRef]
7. Mu, B.; Guo, L.; Liao, J.; Xie, P.; Ding, G.; Lv, Z.; Zhou, Y.; Han, S.; Yan, Y. Near-Infrared Artificial Synapses for Artificial Sensory Neuron System. *Small* **2021**, *17*, 2103837. [CrossRef]
8. Chen, K.; Hu, H.; Song, I.; Gobeze, H.B.; Lee, W.J.; Abtahi, A.; Schanze, K.S.; Mei, J. Organic Optoelectronic Synapse Based on Photon-Modulated Electrochemical Doping. *Nat. Photon.* **2023**, *17*, 629–637. [CrossRef]
9. Dan, S.; Paramanik, S.; Pal, A.J. Introducing Chiro-Optical Activities in Photonic Synapses for Neuromorphic Computing and In-Memory Logic Operations. *ACS Nano* **2024**, *18*, 14457–14468. [CrossRef]
10. Wang, X.; Zhang, L.; Zhao, Y.; Qin, Z.; Hu, B.; Zhang, L.; Jiang, Y.; Wang, Q.; Liang, Z.; Tang, X.; et al. Electro-Optically Configurable Synaptic Transistors With Cluster-Induced Photoactive Dielectric Layer for Visual Simulation and Biomotor Stimuli. *Adv. Mater.* **2024**, *36*, 2406977. [CrossRef]
11. Gentili, P.L.; Rightler, A.L.; Heron, B.M.; Gabbutt, C.D. Extending Human Perception of Electromagnetic Radiation to the UV Region through Biologically Inspired Photochromic Fuzzy Logic (BIPFUL) Systems. *Chem. Commun.* **2016**, *52*, 1474–1477. [CrossRef]
12. Guo, Z.; Liu, J.; Han, X.; Ma, F.; Rong, D.; Du, J.; Yang, Y.; Wang, T.; Li, G.; Huang, Y.; et al. High-Performance Artificial Synapse Based on CVD-Grown WSe_2 Flakes with Intrinsic Defects. *ACS Appl. Mater. Interfaces* **2023**, *15*, 19152–19162. [CrossRef]
13. Huang, M.; Ali, W.; Yang, L.; Huang, J.; Yao, C.; Xie, Y.; Sun, R.; Zhu, C.; Tan, Y.; Liu, X.; et al. Multifunctional Optoelectronic Synapses Based on Arrayed MoS_2 Monolayers Emulating Human Association Memory. *Adv. Sci.* **2023**, *10*, 2300120. [CrossRef]
14. Tang, H.; Anwar, T.; Jang, M.S.; Tagliabue, G. Light-Intensity Switching of Graphene/WSe_2 Synaptic Devices. *Adv. Sci.* **2024**, *11*, 2309876. [CrossRef]
15. Yu, J.; Yang, X.; Gao, G.; Xiong, Y.; Wang, Y.; Han, J.; Chen, Y.; Zhang, H.; Sun, Q.; Wang, Z.L. Bioinspired Mechano-Photonic Artificial Synapse Based on Graphene/MoS_2 Heterostructure. *Sci. Adv.* **2021**, *7*, eabd9117. [CrossRef]
16. Raza, W.; Ahmad, K.; Alvarado, F.G.; Oh, T.H. Progress in 2D MoS_2-Based Advanced Materials for Hydrogen Evolution and Energy Storage Applications. *Inorganics* **2025**, *13*, 47. [CrossRef]
17. Kalantar-zadeh, K.; Ou, J.Z.; Daeneke, T.; Strano, M.S.; Pumera, M.; Gras, S.L. Two-Dimensional Transition Metal Dichalcogenides in Biosystems. *Adv. Funct. Mater.* **2015**, *25*, 5086–5099. [CrossRef]
18. Zhao, Y.; Yu, H.B.; Zhao, C.Y.; Kong, D.N.; Wang, D.N.; Fu, L.Y.; Hu, Q.M.; Li, D.; Zang, T.Y.; Zheng, S.J.; et al. Anisotropy and Synaptic Plasticity in CrSBr/WSe_2 Heterojunction for Advanced Neural Network Applications. *Rare Met.* **2025**. [CrossRef]
19. Chen, Z.; Li, Z.; Zhang, M.; Wang, Y.; Zhang, S.; Cheng, Y. Preparation of Non-Noble Metal Catalyst $FeCo_2O_4$/MoS_2 for Production of Hydrogen and Oxygen by Electrochemical Decomposition of Water. *Inorganics* **2024**, *12*, 229. [CrossRef]
20. Mak, K.F.; Lee, C.; Hone, J.; Shan, J.; Heinz, T.F. Atomically Thin MoS_2: A New Direct-Gap Semiconductor. *Phys. Rev. Lett.* **2010**, *105*, 136805. [CrossRef]

21. He, Y.L.; Yan, J.H.; Yang, Y.T.; Lu, Y.X.; Liu, N.; Chen, P.; Liu, X.F.; Qiu, J.R.; Xu, B.B. Achieving Enhanced Linear and Nonlinear Optical Absorption in a $(PEA)_2PbI_4/WS_2$ Heterojunction by Efficient Energy Transfer. *Rare Met.* **2025**. [CrossRef]
22. Teli, A.M.; Mane, S.M.; Mishra, R.K.; Jeon, W.; Shin, J.C. Unveiling the Electrocatalytic Performances of the Pd-MoS_2 Catalyst for Methanol-Mediated Overall Water Splitting. *Inorganics* **2025**, *13*, 21. [CrossRef]
23. Dhankhar, D.; Li, R.; Nagpal, A.; Chen, J.; Cesario, T.C.; Rentzepis, P.M. Extending Human Vision to Infrared and Ultraviolet Light: A Study Using Micro-Particles and Fluorescent Molecules. *IEEE Access* **2020**, *8*, 73890–73897. [CrossRef]
24. Das, S.; Pal, V.; Mukherjee, S.; Das, S.; Tiwary, C.S.; Ray, S.K. Multi-Wavelength Optoelectronic Synaptic Transistors Based on Transition Metal Telluride-Sulfide Heterostructures. *Adv. Opt. Mater.* **2024**, *12*, 2400037. [CrossRef]
25. Hu, Y.; Yang, H.; Huang, J.; Zhang, X.; Tan, B.; Shang, H.; Zhang, S.; Feng, W.; Zhu, J.; Zhang, J.; et al. Flexible Optical Synapses Based on In_2Se_3/MoS_2 Heterojunctions for Artificial Vision Systems in the Near-Infrared Range. *ACS Appl. Mater. Interfaces* **2022**, *14*, 55839–55849. [CrossRef]
26. Tan, F.; Chang, C.; Zhang, N.; An, J.; Liu, M.; Zhao, X.; Che, M.; Liu, Z.; Shi, Y.; Li, Y.; et al. Physisorption-Assistant Optoelectronic Synaptic Transistors Based on Ta_2NiSe_5/SnS_2 Heterojunction from Ultraviolet to near-Infrared. *Light. Sci. Appl.* **2025**, *14*, 122. [CrossRef]
27. Zhai, Y.; Zhou, Y.; Yang, X.; Wang, F.; Ye, W.; Zhu, X.; She, D.; Lu, W.D.; Han, S.T. Near Infrared Neuromorphic Computing via Upconversion-Mediated Optogenetics. *Nano Energy* **2020**, *67*, 104262. [CrossRef]
28. Jeong, B.H.; Lee, J.; Ku, M.; Lee, J.; Kim, D.; Ham, S.; Lee, K.T.; Kim, Y.B.; Park, H.J. RGB Color-Discriminable Photonic Synapse for Neuromorphic Vision System. *Nano-Micro Lett.* **2025**, *17*, 78. [CrossRef]
29. Pan, Y.; Wang, Y.; Ye, M.; Quhe, R.; Zhong, H.; Song, Z.; Peng, X.; Yu, D.; Yang, J.; Shi, J.; et al. Monolayer Phosphorene–Metal Contacts. *Chem. Mat.* **2016**, *28*, 2100–2109. [CrossRef]
30. Somvanshi, D.; Jit, S. Advances in 2D Materials Based Mixed-Dimensional Heterostructures Photodetectors: Present Status and Challenges. *Mater. Sci. Semicond. Process* **2023**, *164*, 107598. [CrossRef]
31. Dixit, V.; Nair, S.; Joy, J.; Vyas, C.U.; Patel, A.B.; Chauhan, P.; Sumesh, C.K.; Narayan, S.; Jha, P.K.; Solanki, G.K.; et al. Growth and Application of WSe_2 Single Crystal Synthesized by DVT in Thin Film Hetero-Junction Photodetector. *Eur. Phys. J. B* **2019**, *92*, 118. [CrossRef]
32. Hao, Y.; Zhang, S.; Fan, C.; Liu, J.; Hao, S.; Lu, X.; Zhou, J.; Qiu, M.; Li, J.; Hao, G. Te Nanomesh-Monolayer WSe_2 Vertical van Der Waals Heterostructure for High-Performance Photodetector. *Appl. Phys. Lett.* **2025**, *126*, 031904. [CrossRef]
33. Rana, J.S.; Jit, S. A Low-Cost Solution-Processed PTB7-Based MSM Visible Photodetector. *IEEE Trans. Electron. Devices* **2024**, *71*, 1208–1213. [CrossRef]
34. Grillo, A.; Di Bartolomeo, A. A Current–Voltage Model for Double Schottky Barrier Devices. *Adv. Electron. Mater.* **2021**, *7*, 2000979. [CrossRef]
35. Singh, S.; Jit, S. Thermally Grown $MoSe_2$ Thin Film Based MSM Broadband Photodetector. *IEEE Photonics Technol. Lett.* **2024**, *36*, 1105–1108. [CrossRef]
36. Pataniya, P.; Zankat, C.K.; Tannarana, M.; Sumesh, C.K.; Narayan, S.; Solanki, G.K.; Patel, K.D.; Pathak, V.M.; Jha, P.K. Paper-Based Flexible Photodetector Functionalized by WSe_2 Nanodots. *ACS Appl. Nano Mater.* **2019**, *2*, 2758–2766. [CrossRef]
37. Zhao, W.; Ghorannevis, Z.; Amara, K.K.; Pang, J.R.; Toh, M.; Zhang, X.; Kloc, C.; Tan, P.H.; Eda, G. Lattice Dynamics in Mono- and Few-Layer Sheets of WS_2 and WSe_2. *Nanoscale* **2013**, *5*, 9677. [CrossRef]
38. Wen, D.P.; Chen, P.; Liang, Y.; Mo, X.M.; Pan, C.F. Regulated Polarization Degree of Upconversion Luminescence and Multiple Anti-Counterfeit Applications. *Rare Met.* **2024**, *43*, 2172–2183. [CrossRef]
39. Zheng, W.; Huang, P.; Gong, Z.; Tu, D.; Xu, J.; Zou, Q.; Li, R.; You, W.; Bünzli, J.-C.G.; Chen, X. Near-Infrared-Triggered Photon Upconversion Tuning in All-Inorganic Cesium Lead Halide Perovskite Quantum Dots. *Nat. Commun.* **2018**, *9*, 3462. [CrossRef]
40. Tan, D.; Zhang, Z.; Shi, H.; Sun, N.; Li, Q.; Bi, S.; Huang, J.; Liu, Y.; Guo, Q.; Jiang, C. Bioinspired Artificial Visual-Respiratory Synapse as Multimodal Scene Recognition System with Oxidized-Vacancies MXene. *Adv. Mater.* **2024**, *36*, 2407751. [CrossRef]
41. Wang, Y.; Shan, W.; Li, H.; Zhong, Y.; Wustoni, S.; Uribe, J.; Chang, T.; Musteata, V.E.; Yue, W.; Ling, H.; et al. An Optoelectrochemical Synapse Based on a Single-Component n-Type Mixed Conductor. *Nat. Commun.* **2025**, *16*, 1615. [CrossRef]
42. Wang, L.; Wang, L.; Ye, X.Y.; Xu, X.H.; Shang, L.Y.; Li, Y.W.; Zhang, J.Z.; Zhu, L.Q.; Hu, Z.G. Thermally Modulated Photoelectronic Synaptic Behavior in HfS_2/VO_2 Heterostructure. *Rare Met.* **2024**, *43*, 3798–3809. [CrossRef]
43. Liu, Z.; Wang, Y.; Zhang, Y.; Sun, S.; Zhang, T.; Zeng, Y.; Hu, L.; Zhuge, F.; Lu, B.; Pan, X.; et al. Harnessing Defects in SnSe Film via Photo-Induced Doping for Fully Light-Controlled Artificial Synapse. *Adv. Mater.* **2025**, *37*, 2410783. [CrossRef]
44. Zheng, X.; Dong, M.; Li, Q.; Wang, L.; Liu, Y.; Di, X.; Hua, Q.; Wang, L.; Meng, J.; Li, Z. Retina-Inspired Artificial Synapses with UV Modulated and Immediate Switchable Plasticity. *Adv. Funct. Mater.* **2025**, 2420612. [CrossRef]
45. Liu, X.; Huang, M.; Zou, X.; Ali, W.; Rehman, S.U.; Li, J.; Li, Z.; Xiang, L.; Pan, A. Alcohol-Sensitive MoS_2 Optoelectronic Synapses for Mimicking Human-like Visual Adaptation. *InfoMat* **2025**, e70019. [CrossRef]
46. Gu, X.; Zhou, M.; Zhao, Y.; Zhang, Q.; Zhang, J.; Huang, Y.; Lu, S. Realize Ultralow-Energy-Consumption Photo-Synaptic Device Based on a Single (Al, Ga)N Nanowire for Neuromorphic Computing. *Nano Res.* **2024**, *17*, 1933–1941. [CrossRef]

47. Gong, Y.; Xie, P.; Xing, X.; Lv, Z.; Xie, T.; Zhu, S.; Hsu, H.H.; Zhou, Y.; Han, S.T. Bioinspired Artificial Visual System Based on 2D WSe_2 Synapse Array. *Adv. Funct. Mater.* **2023**, *33*, 2303539. [CrossRef]
48. Gracheva, E.O.; Ingolia, N.T.; Kelly, Y.M.; Cordero-Morales, J.F.; Hollopeter, G.; Chesler, A.T.; Sánchez, E.E.; Perez, J.C.; Weissman, J.S.; Julius, D. Molecular Basis of Infrared Detection by Snakes. *Nature* **2010**, *464*, 1006–1011. [CrossRef]
49. Pang, X.; Wang, Y.; Zhu, Y.; Zhang, Z.; Xiang, D.; Ge, X.; Wu, H.; Jiang, Y.; Liu, Z.; Liu, X.; et al. Non-Volatile Rippled-Assisted Optoelectronic Array for All-Day Motion Detection and Recognition. *Nat. Commun.* **2024**, *15*, 1613. [CrossRef]
50. Luan, W.; Zhao, Z.; Li, H.; Zhai, Y.; Lv, Z.; Zhou, K.; Xue, S.; Zhang, M.; Yan, Y.; Cao, Y.; et al. Near-Infrared Response Organic Synaptic Transistor for Dynamic Trace Extraction. *J. Phys. Chem. Lett.* **2024**, *15*, 8845–8852. [CrossRef]
51. Chen, P.; Pan, J.; Gao, W.; Wan, B.; Kong, X.; Cheng, Y.; Liu, K.; Du, S.; Ji, W.; Pan, C.; et al. Anisotropic Carrier Mobility from 2H WSe_2. *Adv. Mater.* **2022**, *34*, 2108615. [CrossRef]
52. Wen, D.; Zuo, S.; Huang, C.; Tan, Z.; Lu, F.; Liang, Y.; Mo, X.; Lin, T.; Cao, S.; Qiu, J.; et al. Tunable Excitation Polarized Upconversion Luminescence and Reconfigurable Double Anti-Counterfeiting from Er^{3+} Doped Single Nanorods. *Adv. Opt. Mater.* **2023**, *11*, 2301126. [CrossRef]

Disclaimer/Publisher's Note: The statements, opinions and data contained in all publications are solely those of the individual author(s) and contributor(s) and not of MDPI and/or the editor(s). MDPI and/or the editor(s) disclaim responsibility for any injury to people or property resulting from any ideas, methods, instructions or products referred to in the content.